JGR Atmospheres

RESEARCH ARTICLE
10.1029/2023JD039121

Atmospheric Wave Radiation by Vibrations of an Ice Shelf

Oleg A. Godin[1], Nikolay A. Zabotin[2], and Liudmila Zabotina[2]

[1]Department of Physics, Naval Postgraduate School, Monterey, CA, USA, [2]Department of Electrical, Computer, and Energy Engineering, University of Colorado at Boulder, Boulder, CO, USA

Key Points:

- Vibrations of large ice shelves radiate atmospheric waves that can travel in a wide range of directions from near-horizontal to near-zenith
- Simple, numerically efficient model is developed of atmospheric wave generation by finite sources at the ground level
- With the surface vibrations' spectrum as the input, the model quantifies atmospheric perturbations from the troposphere to the thermosphere

Correspondence to:
O. A. Godin,
oagodin@nps.edu

Citation:
Godin, O. A., Zabotin, N. A., & Zabotina, L. (2023). Atmospheric wave radiation by vibrations of an ice shelf. *Journal of Geophysical Research: Atmospheres*, *128*, e2023JD039121. https://doi.org/10.1029/2023JD039121

Received 19 APR 2023
Accepted 21 OCT 2023

Abstract Lidar and radar observations of persistent atmospheric wave activity in the Antarctic atmosphere motivate investigation of generation of acoustic-gravity waves (AGWs) by vibrations of ice shelves and exploiting their possible ionospheric manifestations as a source of information about the ice shelves' conditions and stability. A mathematical model of the waves radiated by vibrations of a finite area of the lower boundary of the atmosphere is developed in this paper by extending to AGWs an efficient, numerically exact approach that was originally developed in seismology and underwater acoustics. The model represents three-dimensional wave fields as Fourier integrals of numerical or analytical solutions of a one-dimensional wave equation and accounts for the source directionality, AGW refraction and diffraction, and the wind-induced anisotropy of wave dissipation. Application of the model to the generation of atmospheric waves in Antarctica by free vibrations of the Ross Ice Shelf reveals a complex three-dimensional structure of the AGW field and elucidates the impact of various environmental factors on the wave field. The intricate variation of the wave amplitude with altitude and in the horizontal plane is shaped by the spatial spectrum of the ice surface vibrations and the temperature and wind velocity stratification from the troposphere to the mesosphere. It is found that the waves due to the low-order modes of the free oscillations of the Ross Ice Shelf, which have periods of the order of several hours, can transport energy to the middle and upper atmosphere in a wide range of directions from near-horizontal to near-vertical.

Plain Language Summary This research paper paves the way to infer the conditions and stability of ice shelves in Antarctica by looking at unusual wave activity in the atmosphere. The researchers have developed a mathematical model to understand how these waves, called acoustic-gravity waves (AGWs), are created by the vibrations of ice shelves. The model is based on a method previously used in seismology and underwater acoustics and accounts for various factors that affect the waves, such as the properties of the source, the way the waves bend and spread due to wind, and how they dissipate. The researchers applied this model to study the atmospheric waves generated by vibrations of the Ross Ice Shelf in Antarctica. The results show a complex 3D structure of the AGW field, highlighting the impact of different environmental factors on the wave activity. The variation in wave amplitude depends on the ice surface vibrations and the temperature and wind conditions at different heights in the atmosphere. The study found that waves with periods of several hours can transfer energy from the ice shelf to the middle and upper atmosphere in various directions. This new approach could help scientists better understand the conditions and stability of ice shelves in the future.

1. Introduction

It has been long recognized that dominant nontidal atmospheric wave activity originates from moist convection, transient weather phenomena, shear flow instabilities, jets, atmospheric fronts, and interaction of winds with the Earth's topography (Alexander et al., 2016; Fritts & Alexander, 2003; Geller et al., 2013; Gossard & Hooke, 1975; Medvedev et al., 2023; Plougonven & Zhang, 2014; Vadas et al., 2018; Vincent et al., 2013), with additional significant contributions in polar regions due to auroras (Hunsucker, 1982; Oyama & Watkins, 2012). Less advanced is the understanding and quantitative description of the waves that are generated at the lower boundary of the atmosphere due to seismic events (Astafyeva et al., 2013; Lognonné, 2010; Maruyama et al., 2012; Meng et al., 2019), volcano eruptions (Kulichkov et al., 2022; Lin et al., 2022; Matoza et al., 2022; Watada & Kanamori, 2010; Wright et al., 2022), and surface gravity waves in the ocean, including tsunamis (Artru et al., 2005; Garcia et al., 2014; Godin et al., 2015; Hickey et al., 2009; Occhipinti et al., 2006; Zabotin et al., 2016).

Investigation of vibrations of ice shelves and ice sheets as another ground-level source of the long atmospheric waves, which can reach the middle and upper atmosphere (Godin & Zabotin, 2016; Godin et al., 2020), were motivated by recent lidar observations of the unusual, persistent atmospheric wave activity in Antarctica (Chen

et al., 2016; Chu et al., 2018; Zhao et al., 2017). The observations were made at McMurdo, Antarctica at the edge of the Ross Ice Shelf (RIS) and found high-amplitude acoustic-gravity waves (AGWs) in a wide altitude range from the stratosphere to lower thermosphere. The hypothesis that the persistent atmospheric wave activity was generated by resonant vibrations of the RIS was shown to explain several key features of the observations, including frequency band, vertical wavelength range, and weak variation of the vertical wavelength with height (Godin & Zabotin, 2016). A direct experimental confirmation of the relation between vertical displacement of the ice surface with atmospheric waves with periods of 2 hours and longer was recently obtained (Zabotin et al., 2023) by combining radar measurements of the wave characteristics at the ionospheric altitudes using a Dynasonde system installed at the Jang Bogo Station, Antarctica (Kim et al., 2022; Kwon et al., 2018) with the measurements of the RIS vibrations using a network of seismometers (Bromirski et al., 2015; Diez et al., 2016).

The amplitude and spatial structure of the atmospheric wave field generated by vibrations of an ice shelf is a result of a complex interplay of the temperature and wind velocity stratification in the atmosphere, which combine to control AGW refraction and dissipation, with the temporal and spatial spectra of the forcing at the lower boundary of the atmosphere, which determine wave source directionality and affect wave diffraction. The goal of this paper is to develop an efficient quantitative model of the AGWs radiated by vibrations of ice shelves or ice sheets and, more generally, by generic coherent vibrations of the ground surface within a finite area.

Different approaches have been explored in the literature to model the atmospheric waves generated by various physical processes at and below the lower boundary of the atmosphere (Averbuch et al., 2020; Godin et al., 2020; Hickey et al., 2009; Kanamori et al., 1994; Occhipinti et al., 2006; Press & Harkrider, 1962; Snively, 2013; Watada, 2009; Wu et al., 2020), with the most attention directed toward transient and impulsive wave sources. Here we extend to acoustic-gravity waves (AGWs) in a horizontally stratified atmosphere the approach that has been developed for sound and elastic waves in layered fluid and elastic solid media and is based on calculating monochromatic wave fields in two and three dimensions as Fourier integrals of solutions of one-dimensional wave equations (DiNapoli & Deavenport, 1980; Fuchs & Müller, 1971; Schmidt & Glattetre, 1985; Schmidt & Tango, 1986). Because of its computational efficiency, versatility, and ability to simultaneously handle wave propagation in every direction from horizontal to vertical from the source, the approach has found numerous applications in underwater acoustics and seismo-acoustics, where it is known as either the fast field algorithm or the wavenumber integration technique, see (Aki & Richards, 2002, Chap. 9; Brekhovskikh & Godin, 1999, Chap. 1; Jensen et al., 2011, Chap. 4) and references therein. In the context of atmospheric waves, the wavenumber integration approach appears to be especially well suited for numerical simulations of waves due to harmonic sources. In this paper, the approach is applied to modeling atmospheric AGWs that are generated by free vibrations of large ice shelves, the energy of which is concentrated around a set of discrete natural frequencies (Godin & Zabotin, 2016; Holdsworth & Glynn, 1978, 1981; Papathanasiou et al., 2019; Sergienko, 2013; Zabotin et al., 2023). As discussed below, an extension of the acoustic wave number integration method to AGWs requires its significant modifications, which are due to the AGWs having trace speeds that may be comparable to the wind speed, and a qualitative difference between the acoustic dispersion relation and the dispersion equation of long-period AGWs.

The paper is organized as follows. In Section 2, the two- and three-dimensional problems of modeling the AGW field in the atmosphere due to vibrations of its lower boundary is reduced to solving one-dimensional wave equations, and numerical aspects of implementation of such an approach are discussed. The resulting mathematical model is applied in Section 3 to investigate the atmospheric waves generated by a single mode of free vibrations of the RIS. The conditions leading to the unusual, near-vertical propagation of long-period atmospheric AGWs (often referred to as gravity waves in the literature) are identified in Section 4. Section 5 summarizes our findings.

2. Mathematical Model of Radiation of Acoustic-Gravity Waves (AGWs)

Consider acoustic-gravity waves (AGWs) in an atmosphere with sound speed c, background flow velocity (wind) $\mathbf{u}$, and density ρ in a uniform gravity field with acceleration g. Mathematical models of AGW excitation usually assume either a point source (Adam, 1977; Godin & Fuks, 2012; Kanamori et al., 1994; Pierce, 1963) or an infinite, spatially periodic source (Godin et al., 2015; Watada, 2009). These idealizations are appropriate, respectively, when the source dimensions are either much smaller or much larger than the AGW wavelength. In the problem of AGW generation by low-order modes of vibrations of ice shelves, horizontal wavelength of the vibrations and the spatial extent of the ice shelf can be of the same order of magnitude. With the source aperture

comparable to the wavelength, AGW diffraction effects are expected to play a significant role. Here, we develop a mathematical description of linear atmospheric waves due to a finite source at the lower boundary of the atmosphere.

Below, a Cartesian coordinate system is used with horizontal coordinates x and y and a vertical coordinate (altitude) z. The vertical coordinate $z = 0$ on the ice-atmosphere interface, or ground level, and increases upward. AGWs add time- and coordinate-dependent perturbations to the background atmospheric parameters c, ρ, and $\mathbf{u}$. These parameters vary with altitude but are assumed to be independent of the horizontal coordinates and time t. It is also assumed that the wind velocity $\mathbf{u}$ has no vertical component.

2.1. Integral Representation of the Wave Field

Let AGW be generated by monochromatic oscillations of the lower boundary $z = 0$ of the atmosphere. Vertical displacement χ of the boundary is

$$\chi(x, y, t) = w_0(x, y)\exp(-i\omega t), \tag{1}$$

where ω is the frequency of the oscillations, and $w_0(x, y)$ is an integrable function with the spatial spectrum

$$\Phi(\xi_x, \xi_y) = (2\pi)^{-2}\int_{-\infty}^{\infty}\int_{-\infty}^{\infty} w_0(x, y)\exp(-i\xi_x x - i\xi_y y)d\xi_x d\xi_y. \tag{2}$$

Here and below complex notation for the wave field quantities is used. The time dependence exp(–$i\omega t$) is assumed throughout and will be suppressed.

The wave field at $z > 0$ can be viewed as the superposition of the AGWs that are generated by individual components of the surface displacement with the harmonic dependence $\exp(ik_x x + ik_y y - i\omega t)$ on horizontal coordinates and time. AGW boundary conditions require that the vertical displacement of air at $z = 0$ equals that of the boundary (Godin, 1997; Gossard & Hooke, 1975). Hence, vertical displacements in air at $z \to 0$ have the same spatial spectrum Φ as the oscillations of the lower boundary. These oscillations generate the AGW field in the atmosphere with the vertical displacement

$$w(x, y, z) = \int_{-\infty}^{\infty}\int_{-\infty}^{\infty} W(\mathbf{k}, z)\Phi(k_x, k_y)\exp(ik_x x + ik_y y)dk_x dk_y, \tag{3}$$

where $\mathbf{k} = (k_x, k_y, 0)$ and $W(\mathbf{k}, z)$ have the meaning of the horizontal wave vector and the vertical dependence of the particle displacement in the "quasi-plane" AGW with the plane-wave dependence $\exp(ik_x x + ik_y y)$ on horizontal coordinates; $\exp(ik_x x+ik_y y)W(\mathbf{k},z)$ is the wave field in the atmosphere that is generated by a plane wave with vertical displacement $\exp(ik_x x + ik_y y)$ propagating along the ground level. The function $W(\mathbf{k}, z)$ satisfies the boundary condition $W(\mathbf{k}, 0) = 1$ at $z = 0$ and the one-dimensional AGW wave equation (Godin, 2015)

$$\frac{d}{dz}\left[\frac{\rho\omega_d^2 dW/dz}{\omega_d^2 c^{-2} - k^2}\right] + \left[\omega_d^2 - \frac{g^2k^2}{\omega_d^2 - k^2c^2} - \frac{g}{\rho}\frac{d}{dz}\left(\frac{\rho k^2}{\omega_d^2 c^{-2} - k^2}\right)\right]\rho W = 0. \tag{4}$$

The quasi-plane wave either carries wave energy upward or vanishes at $z\to\infty$. Here $k^2 = k_x^2 + k_y^2$, and $\omega_d = \omega - \mathbf{k}\cdot\mathbf{u}$ is the intrinsic frequency. It has the meaning of the wave frequency in the reference frame moving with the local wind.

In the simplified, two-dimensional (2-D) problem in the xz plane, where the boundary displacement χ is a function of only one horizontal coordinate, x,

$$w_0 = \int_{-\infty}^{\infty}\Phi_1(k_x)\exp(ik_x x)dk_x, \tag{5}$$

and the AGW field in the atmosphere is independent of the coordinate y. Then, instead of two-fold integral in Equation 3, the vertical displacement in AGWs at $z > 0$ is given by the equation

$$w(x,z)=\int_{-\infty}^{\infty}W(\mathbf{k},z)\Phi_1(k_x)\exp(ik_x x)dk_x, \tag{6}$$

where $\mathbf{k}=(k_x,0,0)$ and W satisfies the same wave equation Equation 4 and boundary conditions as in the 3-D problem.

The integral representations of the AGW field in 2-D and 3-D problems, Equations 3 and 6, are analogous to the representations in acoustics and optics of the field either generated by a finite source or diffracted through a finite aperture (Godin, 1984; Pierce, 2019). The computational advantage of these integral representations over alternative representations involving integration of the Green's function over the aperture, stems from the fact that quasi-plane waves are much easier to calculate in layered media than the Green's functions. An additional advantage of the integral representations Equations 3 and 6 in application to AGWs is that quasi-plane waves do not have the singularities that the AGW Green's functions have away from the wave source (Adam, 1977).

As a function of k_x, $W(\mathbf{k},z)$ in the integrand of Equations 3 and 6 may have poles, including the poles associated with the acoustic and buoyancy resonances of the atmosphere (Godin et al., 2020; Watada & Kanamori, 2010) and Lamb waves (Godin, 2012; Gossard & Hooke, 1975; Kubota et al., 2022). Numerical aspects of modeling sound fields in layered media using acoustic counterparts of Equations 3 and 6 have been perfected in underwater acoustics under the names of wavenumber integration and fast field algorithms (Jensen et al., 2011). These numerical approaches, including techniques for dealing with the poles of the integrand that correspond to guided waves (also known as ducted waves), readily translate to the AGW problem.

2.2. Group Velocity and Ray Geometry

When the temperature, wind speed, and composition of the atmosphere vary gradually with altitude, AGWs can be mathematically described in the WKB approximation (Budden & Smith, 1976; Godin, 2015). The approximation represents a systematic asymptotic solution of equations of hydrodynamics for linear waves. It should be distinguished from ad hoc approximations (Einaudi & Hines, 1970; Fritts & Alexander, 2003; Gossard & Hooke, 1975; Jones & Georges, 1976; Pitteway & Hines, 1965) using the same name. The WKB approximation leads to the following AGW dispersion equation:

$$m^2=\frac{\omega_d^2}{c^2}-\frac{1}{4h^2}+k^2\frac{N_0^2-\omega_d^2}{\omega_d^2}. \tag{7}$$

Here m is the vertical component of the AGW wave vector (also referred to as the vertical wavenumber), $h=c^2/\gamma g$ is the scale height, γ is the ratio of specific heats at constant pressure and constant volume, and $N_0^2=(\gamma-1)g^2/c^2$ is close to but generally different from the buoyancy frequency squared, $N^2=g\rho^{-1}d\rho/dz-g^2c^{-2}$. The function $N_0(z)$ in Equation 7 has the meaning of the smoothed vertical profile of the buoyancy frequency $N(z)$.

The necessary condition of validity of the WKB approximation can be written as the inequality $|m^{-2}\,dm/dz|\ll 1$ (Godin, 2015). In the WKB approximation [more accurately, in the first WKB approximation, see (Godin, 2015)] the one-dimensional AGW wave equation has two linearly independent solutions,

$$\begin{aligned}W(\mathbf{k},z)=&\sqrt{\frac{\left(c^{-2}-k^2\omega_d^{-2}\right)\rho_0 m_0}{\left(c_0^{-2}-k^2\omega_{d\,0}^{-2}\right)\rho m}}\exp(i\varphi)\\&\times\exp\left(i\int_0^z\frac{dz_1}{2m}\left[\frac{d}{dz_1}\left(\frac{1}{2h}-\frac{gk^2}{\omega_d^2}\right)-\left(\frac{1}{2h}-\frac{gk^2}{\omega_d^2}\right)\frac{d}{dz_1}\ln\left(\frac{h}{c^2}-\frac{k^2h}{\omega_d^2}\right)\right]\right),\end{aligned} \tag{8}$$

where $m=\pm\sqrt{m^2}$, subscript 0 indicates the values of respective quantities at $z=0$, and φ is the phase integral:

$$\varphi(\mathbf{k},z)=\exp\left(i\int_0^z m\,dz_1\right). \tag{9}$$

Note that waves with $m^2<0$ are evanescent.

When $m^2 \geq 0$, AGWs with wave vector (k_x, k_y, m) carry the wave energy from the source along the rays in the direction of the group speed $\mathbf{c}_g = (\partial\omega/\partial k_x, \partial\omega/\partial k_y, \partial\omega/\partial m)$. It follows from Equation 7 that

$$\mathbf{c}_g = \mathbf{u} + \frac{1}{\omega_d}\left(\frac{k^2 N_0^2}{\omega_d^4} - \frac{1}{c^2}\right)^{-1}\left(\frac{N_0^2 - \omega_d^2}{\omega_d^2}\mathbf{k} - m\hat{\mathbf{z}}\right), \tag{10}$$

where $\hat{\mathbf{z}}$ is a unit vertical vector in the direction of increasing altitude z. The sign of vertical component $c_{g,z}$ of the group velocity is opposite for the waves with $m = \sqrt{m^2}$ and $m = -\sqrt{m^2}$. Note that $c_{g,z} > 0$ and the wave propagates toward increasing altitudes when $m > 0$ for AGWs on the acoustic branch (i.e., at $\omega_d > \gamma g/2c$) and when $m < 0$ for AGWs on the gravity (or buoyancy) branch (i.e., at $0 < \omega_d < N_0$) (Godin, 2015; Gossard & Hooke, 1975).

Both m and $\mathbf{c}_g$ are constant, and the rays are straight lines in the atmosphere with constant sound speed and composition and uniform wind. The rays are generally 3-D curves in stratified atmosphere and may have turning points $z = z_t$, where the signs of m and the vertical component of the group speed change. Ray geometry follows from Equation 10. Let the two-dimensional vector $\mathbf{r}_h(z, \mathbf{k})$ give the horizontal coordinates of the ray at altitude z. Then, for any two altitudes z_1 and z_2 we have

$$\mathbf{r}_h(z_1, \mathbf{k}) - \mathbf{r}_h(z_2, \mathbf{k}) = \int_{z_2}^{z_1} \frac{(c_{g,x}, c_{g,y}, 0)}{c_{g,z}} dz = \int_{z_2}^{z_1} \left[\left(\frac{\omega_d}{c^2} - \frac{k^2 N_0^2}{\omega_d^3}\right)\mathbf{u} + \frac{\omega_d^2 - N_0^2}{\omega_d^2}\mathbf{k}\right]\frac{dz}{m} \tag{11}$$

on any segment of the ray without turning points.

Equations 7–11 are used below for physical interpretation of the numerical results and, where appropriate, to increase computational efficiency of the mathematical model based on the integral representations Equations 3 and 6 of the AGW field.

2.3. AGWs in a Dissipative Atmosphere

Wave Equation 4 describes AGWs in an ideal fluid and disregards dissipation of atmospheric waves. Full description of dissipation of linear AGWs due to viscosity and thermal conductivity requires solution of coupled partial differential equations expressing mass, momentum, and energy balance as well as equation of state of the atmosphere (e.g., Godin, 2014). AGWs prove to be coupled to the evanescent viscous and entropy waves, which leads to a high-order wave equation. However, the coupling is weak in fluids with gradually varying parameters, and, as long as the relative loss of wave energy per wavelength is small, the dominant effect of dissipative processes on the wave field can be described by assigning complex values to the vertical component m of the wave vector in the phase integral (9). The effective value of the vertical component of the AGW wave vector in viscous, thermally conductive gas is given by the equation (Godin, 2014; Golitsyn, 1965)

$$m_e^2 = m^2 + iM, M = \frac{1}{\omega_d \rho}\left[B_1\eta + B_2\zeta + B_3\frac{(\gamma - 1)\kappa}{C_p}\right], \tag{12}$$

where C_p, η, ζ, and κ are the specific heat at constant pressure, shear viscosity, bulk viscosity, and thermal conductivity of the gas. In the atmosphere, $\kappa/C_p = 4\gamma\eta/(9\gamma - 5)$ to good accuracy (Sutherland & Bass, 2004).

The coefficients B_1, B_2, and B_3 in Equation 12 are

$$\begin{aligned} B_1 &= \left(\frac{4\omega_d^2}{3c^2} - k^2\frac{N_0^2}{\omega_d^2}\right)\left(\frac{\omega_d^2}{c^2} + k^2\frac{N_0^2}{\omega_d^2}\right) + \frac{5gk^2}{3hc^2} - \frac{k^2}{h^2}, \\ B_2 &= \frac{\omega_d^4 - g^2k^2}{c^4}, B_3 = \left(1 + \frac{gc^2k^2}{\omega_d^4 h} - \frac{g^2k^2}{\omega_d^4}\right)B_2, \end{aligned} \tag{13}$$

if η/ρ, ζ/ρ, and κ/ρ are assumed to be slowly varying functions of altitude (Godin, 2014; Golitsyn, 1965). If the more realistic assumption is made that η, ζ, and κ are slowly varying functions, so that kinematic viscosity of air increases nearly exponentially with altitude, a different set of coefficients $B_1 = \alpha B_{11}, B_2 = \alpha B_{22}, B_3 = \alpha B_{33}$ arises from the asymptotic analysis of the problem and $M = \alpha M_1$ in Equation 12 (Godin, 2014), where

$$\alpha = k^2 + \left(m - \frac{i}{2h}\right)^2, M_1 = \frac{1}{\omega_d \rho}\left[B_{11}\eta + B_{22}\zeta + B_{33}\frac{(\gamma-1)\kappa}{C_p}\right],$$
$$B_{11} = \frac{4\omega_d^2}{3c^2} - k^2\frac{N_0^2}{\omega_d^2}, B_{22} = \frac{\omega_d^2}{c^2}, B_{33} = \left(1 - \frac{g^2k^2}{\omega_d^4}\right)\frac{\omega_d^2}{c^2}. \quad (14)$$

The wave frequency ω enters Equations 12–14 via the intrinsic frequency ω_d. Note that AGWs with the same frequency ω and the same horizontal wavenumber k experience different absorption in the atmosphere when they propagate in different directions with respect to the local wind (Godin, 2014).

Asymptotic results Equations 12 and 13 will be reproduced by the solutions of the AGW wave equation if viscosity- and thermal conductivity-related terms are introduced in Equation 4 as follows:

$$\frac{d}{dz}\left[\frac{\rho\omega_d^2 dW/dz}{\omega_d^2 c^{-2} - k^2}\right] + \left[\omega_d^2 - \frac{g^2k^2c^{-2} - i\omega_d^2 M}{\omega_d^2 c^{-2} - k^2} - \frac{g}{\rho}\frac{d}{dz}\left(\frac{\rho k^2}{\omega_d^2 c^{-2} - k^2}\right)\right]\rho W = 0. \quad (15)$$

When dissipation is negligible, $M \to 0$ according to Equations 12, and Eq. 15 reduces to Equation 4.

In contrast to Equation 13, Equations 12 and 14 predict that dissipation rates are different for waves propagating up and down (i.e., for different signs of m). This cannot be captured by Equation 15 with any value of M, and a different modification of the AGW wave Equation 4 becomes necessary. The asymptotic results Equations 12 and 14 are reproduced by solutions of the following AGW wave equation:

$$\frac{d}{dz}\left[\frac{\rho\omega_d^2(1 - iM_1)}{\omega_d^2 c^{-2} - k^2}\frac{dW}{dz}\right] + \left[\omega_d^2 - k^2\frac{g^2c^{-2} - i\omega_d^2 M_1}{\omega_d^2 c^{-2} - k^2} - \frac{g}{\rho}\frac{d}{dz}\left(\frac{\rho k^2}{\omega_d^2 c^{-2} - k^2}\right)\right]\rho W = 0. \quad (16)$$

In both Equations 15 and 16, the effects of viscosity and thermal conductivity of the real atmosphere are accounted for by assigning complex values to the coefficients of the second-order differential equation, which are real-valued for AGWs in ideal fluids. The agreement of the modified wave Equations 15 and 16 with the corresponding asymptotic results can be readily verified by deriving respective eikonal equations using the technique described in Godin (2015).

In moving atmosphere AGWs may have critical levels, where the intrinsic frequency $\omega_d = 0$. At the critical level, the trace speed ω/k, that is, the speed with which phase front of the wave moves along a horizontal plane, equals the component $u_k = \mathbf{u}\cdot\mathbf{k}/k$ of the wind velocity in the direction of the horizontal wave vector $\mathbf{k}$. Wind speed needs to be greater or equal to ω/k for the critical level to occur. As the wave approaches its critical level, the vertical component of the wave vector m tends to infinity, $m \approx \pm kN_0/\omega_d$ from Equation 7, and the vertical component of the group speed $\mathbf{c}_g$ Equation 10 vanishes. Coefficients α, B_1, B_3, B_{11}, and B_{33} in Equations 13 and 14 tend to infinity, and Equation 12 predicts very strong dissipation of AGWs in the vicinity of the critical level due to shear viscosity and thermal conductivity of the atmosphere. In the linear asymptotic theory, the AGW is completely dissipated as it approaches the critical level. This is the well-known effect of wave blocking at the critical level (Gossard & Hooke, 1975; Hines, 1960).

2.4. Computational Considerations

Numerical modeling of the AGW field using the 3-D or 2-D integral representations Equations 3 and 6 requires reducing the integration domain in the wavenumber space and the range of altitudes, in which the one-dimensional wave Equation 15 or 16 is solved numerically. Integration over a finite range of horizontal wavenumbers in Equations 3 and 6 is efficiently implemented using the FFT algorithm (Jensen et al., 2011).

In acoustics, large values of the horizontal wavenumber k contribute negligibly to the integrals in Equations 3 and 6 because waves are evanescent, and the function W exponentially decreases with z (Jensen et al., 2011). Indeed, Equation 7 with $g = 0$ gives $m^2 < 0$ when $k^2 > \omega_d^2 c^{-2}$. Here and below we take into account that the wind speed is less than the sound speed in the atmosphere. For AGWs on the acoustic branch, waves also become evanescent at large k according to Equation 7. However, m^2 increases with k^2 on the gravity branch, and short waves remain propagating. Equations 12–14 show that absorption increases rapidly with increasing $k^2$and m^2.

For waves on the gravity branch, the limits of integration must be chosen from the condition that the accumulated wave attenuation is sufficiently large in the spatial domain of interest.

A separate analysis is required for AGWs in moving atmosphere because the intrinsic frequency varies with k: $\omega_d = \omega - ku_k$. According to the dispersion Equation 7, AGWs are strongly evanescent and contribute negligibly to the integrals in Equations 3 and 6 when $k > (2h)^{-1}\left(1 - u_k^2/c^2\right)^{-1/2}$, $k > N_0/|u_k|$, and $k \gg \omega/|u_k|$. In a stratified atmosphere, these conditions should be met at all altitudes, where the AGW field is calculated. In practice, the necessary integration domain is further restricted by the critical level filtering of waves traveling downwind (more accurately, when $u_k > 0$) and by the strong attenuation of short AGWs.

The density of air changes by several orders of magnitude between the ground level and the upper atmosphere, and the solution W of Equations 4, 15 and 16 may increase exponentially with z. Application of general-purpose ordinary differential equation (ODE) solvers to the one-dimensional wave equations is simplified, if balancing of exponentially large and exponentially small terms is avoided by using another dependent variable, the normalized vertical displacement

$$Q(\mathbf{k}, z) = \sqrt{\rho(z)/\rho(0)}W(\mathbf{k}, z), \tag{17}$$

and eliminating ρ from coefficients of the equation, see Godin et al. (2020).

AGW reflection in the upper atmosphere becomes negligible at altitudes above certain altitude H because of the exponential increase of kinematic viscosity and thermal diffusivity with altitude and/or because of decrease in the wind speed and temperature gradients at sufficiently high altitudes. Details of the wind velocity and temperature profiles at $z > H$ have negligible effect on the AGW field at $z < H$. Then, the condition that the wave either vanishes or carries energy to $z \to \infty$ can be reformulated and imposed at $z = H$. We model the non-reflecting half-space $z > H$ as an isothermal and uniformly moving medium with the sound speed, scale height, wind velocity, and other parameters retaining the values these have at $z = H$ in real atmosphere. Solving the wave equation at $z > H$ we find that the solution satisfying the radiation conditions at $z \to \infty$ is $Q = const. \times \exp(im_e z)$, where Im $m_e > 0$ and $m_e{}^2$ is given by Equation 12. With Q known at $z > H$, the boundary conditions of continuity of the Lagrangian pressure perturbation and vertical displacement at $z = H$ (Godin, 1997) can be written as the one-sided boundary condition for the wave field at $z < H$:

$$\frac{1}{Q}\frac{dQ}{dz} = im_e - \frac{1}{2h}\frac{dh}{dz}, z = H - 0. \tag{18}$$

With the boundary condition Equation 18, numerical solution of one-dimensional wave equation is required in the finite interval $0 < z < H$ only. If Equation 15 or 16 are solved with the initial conditions

$$Q_1 = 1, \frac{dQ_1}{dz} = im_e - \frac{1}{2h}\frac{dh}{dz}, z = H - 0 \tag{19}$$

imposed just below the altitude H, then the altitude dependence of the normalized vertical displacement in the quasi-plane wave is

$$Q(\mathbf{k}, z) = Q_1(\mathbf{k}, z)/Q_1(\mathbf{k}, 0). \tag{20}$$

Equations 19 and 20 ensure that the boundary conditions (Equation 18) at the top and $W(\mathbf{k}, z) = 1$ at the bottom of the computation domain are met.

A modified approach is used for the quasi-plane waves that have critical levels. Due to the effect of wave blocking at the critical level discussed in Section 2.3, waves with a particular horizontal wave vector $\mathbf{k}$ contribute to the integrals in Equations 3 and 6 only at the altitudes below their lowest critical level. Then, the altitude H in Equations 18 and 19, where the numerical solution is terminated, can be chosen slightly below the lowest critical level (e.g., where $\omega_d = 0.01\omega$). The function W is replaced with zero at $z > H$. This approach allows one to avoid solving the one-dimensional wave equation around the critical level, which is a singular point for ODEs Equations 4, 15 and 16.

Another way to separate unphysical solutions that describe the waves generated at infinity or at the critical levels is to consider monochromatic waves of frequency ω as the limit at $\Gamma \to +0$ of the waves generated by sources

with gradually increasing amplitude and the time dependence $\exp(\Gamma t - i\omega t)$, where $\Gamma > 0$ (Brekhovskikh & Godin, 1999). With such sources, the waves that arrive from infinity or the critical level and have infinite travel times, have zero amplitude. In practice, assigning a small, positive imaginary part $i\Gamma$ to the wave frequency ω in Equations 4, 15 and 16 reduces sensitivity of the numerical solution to the choice of the upper boundary $z = H$ of the computational domain.

As an alternative to imposing the initial conditions at the top of the computational domain, one can instead impose the initial conditions

$$Q = 1, \frac{dQ}{dz} = im_e - \frac{1}{2h}\frac{dh}{dz}, z = 0 \tag{21}$$

at the ground level. The initial conditions (Equation 21) are exact in isothermal atmosphere with uniform wind and with the dissipation term M in Equation 12 being either constant or negligible near the ground level. The approach expressed by Equation 21 is attractive due to its simplicity, but has limited applicability. It is implied in Equation 21 that there is no appreciable reflections from the wind velocity and temperature gradients. That assumption certainly fails if there exists a turning point between the ground level and the lowest critical level. On the other hand, for realistic temperature and wind velocity profiles such as considered in Section 3, the initial conditions (Equation 21) lead to numerically efficient and sufficiently accurate solutions, when either there are no turning points, or the lowest critical level is located below any turning points. In the latter case, the numerical solution is terminated slightly below the critical level.

3. AGWs Generated by the Ross Ice Shelf (RIS)

In this section, the integral representations of the AGW field in two and three spatial dimensions, Equations 3 and 6, are applied to model the atmospheric waves that are generated by free vibrations of large ice shelves and specifically the RIS. The free vibrations can be represented as a superposition of normal modes with distinct natural frequencies. Below we investigate how the spatial structure of vibrations in a single normal mode, the wind, and the atmospheric stratification combine to produce a complex distribution of AGW energy above the ice shelf.

3.1. Long-Period Oscillations of the RIS

Because of the large dimensions of the RIS, the fundamental mode and other low-order modes of its free oscillations have periods of several hours. To interpret observations of unusual persistent atmospheric wave activity in the RIS vicinity as well as seismic observations of long period RIS vibrations, a simple, analytical model of low-order vibrations of the ice shelf and their excitation by the ocean has been developed in Godin and Zabotin (2016) and Zabotin et al. (2023). RIS is modeled as a homogeneous rectangular plate of constant thickness over ocean of constant depth with a rigid bottom. The ice shelf is grounded on one (southern) side, faces the ocean on the opposite (northern) side, and is supported by solid earth on the other (east and west) sides (Figure 1a). The ice shelf grounding line (the south edge of the ice shelf) is located at $x = 0$. The ice front (the north edge of the ice shelf) is located at $x = L$ (Figure 1b). The east and west edges of the ice shelf are at $y = \pm L_y/2$, $0 < x < L$. Representative values of the RIS horizontal extent, ice thickness H_1, and under-ice water depth H_2 are $L = 550$ km, $L_y = 800$ km, $H_1 = 300$ m, and $H_2 = 400$ m (Figures 1a and 1b).

In this paper, we limit the analysis to the two-dimensional ice shelf vibrations, where the vertical displacement χ of the ice upper surface is uniform along y (i.e., independent of the along-the-front coordinate y), and to vibration periods of less than about 4 hours so that the inertial effects due to Earth rotation can be neglected. The RIS vibrations without dependence on y are two-dimensional in the sense that the ice and water displacements vary with x and z and have both x and z components (Godin & Zabotin, 2016). The structure of the oscillations below $z = 0$ affects the AGW generation indirectly through the natural frequencies and the spatial spectrum of the vertical displacement of the upper surface of the ice shelf. In an individual normal mode of two-dimensional vibrations, w_0 in Equation 1 is

$$w_0(x, y) = \frac{AH_1}{i\xi_1}\left(\cos\xi_1 x - \frac{c_1^2\cos\xi_1 L}{c_2^2\cos\xi_2 L}\cos\xi_2 x\right) \tag{22}$$

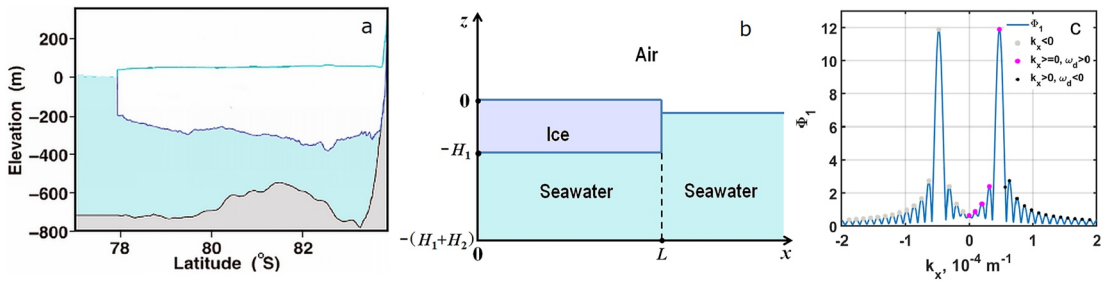

Figure 1. Ross Ice Shelf and its oscillations. (a) A transect of the shelf's ice/water/bedrock geometry along a line roughly orthogonal to the Ross Ice Shelf front [adapted from Bromirski et al. (2015)]. Horizontal axis is compressed by a factor of about 700 compared to the vertical one. (b) Simplified geometry of the ice shelf that is implied in the analytical model of long-period oscillations of the RIS in Godin and Zabotin (2016). The ice shelf grounding line and the ice front are perpendicular to the plane of figure. L is the distance between the grounding line and the ice front. H_1 and H_2 are the thicknesses of the ice and the water-filled cavity beneath the ice. (c) Absolute value of the spatial spectrum Φ_1 of the vertical displacement of the lower boundary of the atmosphere, Equation 25, due to a single mode of two-dimensional RIS oscillations with frequency $\omega = 5.66317{\cdot}10^{-4}$ s^{-1} (oscillation period of about 3.0819 hr). Normalization of the spectrum is arbitrary. Gray dots show positions of the spectrum maxima at $k_x < 0$. Purple and black dots show positions of the spectrum maxima at $k_x \geq 0$, for which the intrinsic frequency of atmospheric waves is, respectively, positive and negative, when the meridional component of the wind velocity $u_x = 10$ m/s.

at $0 < x < L$, $-L_y/2 < y < L_y/2$ and zero otherwise (Godin & Zabotin, 2016). Here A is the mode amplitude, $\xi_1 = \omega/c_1$,$\xi_2 = \omega/c_2$, $c_1 > c_2$ are speeds of "fast" and "slow" long gravity waves in the ice shelf:

$$c_{1,2} = \sqrt{\frac{g}{2}(H_1+H_2)\left[1 \pm \sqrt{1 - \frac{4H_1H_2}{(H_1+H_2)^2}\left(1-\frac{\rho_1}{\rho_2}\right)}\right]}, \tag{23}$$

ρ_1 and ρ_2 are the mass densities of ice and sea water. Equation 22 follows from Equations 22, 27, and 28 in Godin and Zabotin (2016) and the equation $w_0 = -\left(\omega^2\rho_2\right)^{-1} H_1 \partial^2 p/\partial x^2$ [see Equation 6 in Zabotin et al. (2023)] that relates the vertical displacement to pressure perturbation p at $z = 0$. A natural frequency ω of vibrations is determined from the equation

$$\xi_1 \tan \xi_1 L = \xi_2 \tan \xi_2 L. \tag{24}$$

The natural frequencies of free vibrations are also the resonance frequencies of the RIS oscillations forced by ocean waves (Zabotin et al., 2023). The normal mode solution in Equations 22–24 is obtained in the stratified fluid approximation, which for low-order modes is superior to the alternative thin-plate approximation (Zabotin et al., 2023).

When applied to the 2-D model of atmospheric wave generation, Equation 22 gives

$$\Phi_1(k_x) = \frac{AH_1}{2\pi i \xi_1}\left[\Phi_0(\xi_1, k_x) - \frac{c_1^2 \cos \xi_1 L}{c_2^2 \cos \xi_2 L}\Phi_0(\xi_2, k_x)\right], \tag{25}$$

$$\Phi_0(\xi, k) = \frac{e^{0.5i(\xi-k)L}}{k-\xi}\sin\left(\frac{k-\xi}{2}L\right) + \frac{e^{-0.5i(k+\xi)L}}{k+\xi}\sin\left(\frac{k+\xi}{2}L\right) \tag{26}$$

for the spatial spectrum of the vertical displacement of the lower boundary of atmosphere in Equation 5. The value of the spectrum Φ_1 at $k_x = 0$ is proportional to the RIS vertical displacement averaged over the RIS surface. It controls the amplitude of atmospheric waves with horizontal wavenumbers that are small compared to the wavenumbers $\xi_{1,2}$ of fast and slow waves in the ice. We find $\Phi_0(\xi,0) = \xi^{-1}\sin\xi L$ from Equation 26 and

$$\Phi_1(0) = \frac{AH_1 \cos \xi_1 L}{2\pi i \xi_1^2}\left(\tan \xi_1 L - \frac{\xi_1 c_1^2}{\xi_2 c_2^2}\tan \xi_2 L\right) \tag{27}$$

from Equation 25. It follows from the dispersion relation of the ice shelf vibrations, Equation 24, that the quantity in parenthesis on the right side of Equation 27 is zero. Thus, $\Phi_1(0) = 0$, and the average vertical displacements due to slow and fast waves in the ice, each being non-zero, cancel each other. The fact that the average vertical displacement of the RIS equals zero has significant implications for atmospheric wave generation, which are discussed in Section 3.2.

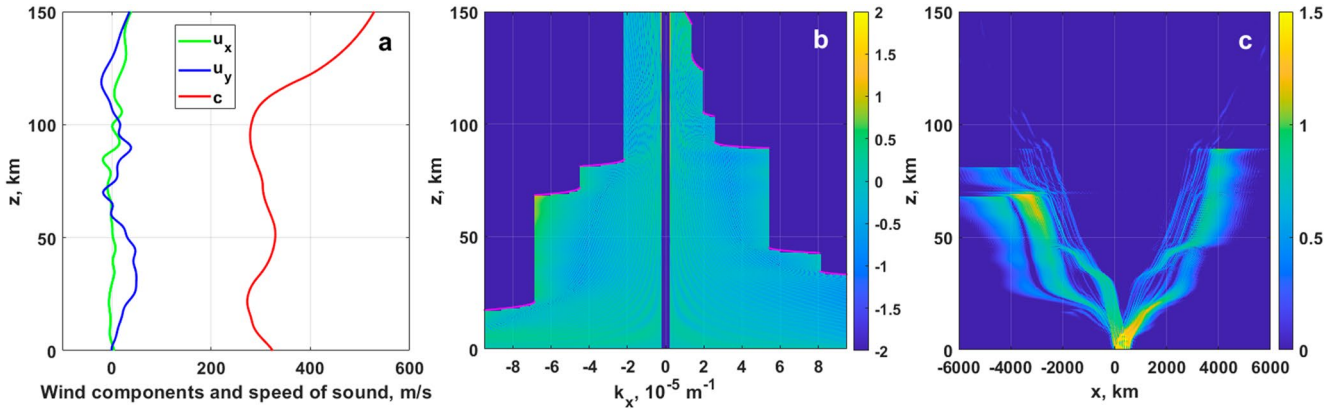

Figure 2. Atmospheric waves generated by one mode of free vibrations of the RIS. (a) Altitude profiles of the sound speed, c, and the meridional, u_x, and zonal, u_y, components of the wind velocity at McMurdo, Antarctica. The wind velocity is provided by the HWM14 model (Drob et al., 2015) for 14:00 UT on 14 July 2014. Sound speed is calculated using the temperature profile as provided by the NRLMSISE-00.2 model (Picone et al., 2002) for the same day and time. (b) Vertical displacement in AGWs with the horizontal wave vector $\mathbf{k} = (k_x, 0, 0)$. The amplitude of the normalized vertical displacement is shown on a logarithmic scale. The vertical displacement $W(\mathbf{k}, z)$ is found numerically by solving Equation 15 with the wind velocity and sound speed profiles shown in panel (a). Magenta lines show the altitudes in the vicinity of the critical levels, where numerical calculations are terminated and above which the waves are rapidly dissipated. (c) Atmospheric wave field in the meridional vertical plane through the center of the RIS. The amplitude of the normalized vertical displacement is shown by color on logarithmic scale. The values below $10^{-1.5}$ of the maximum amplitude are shown in dark blue color. The vertical displacement is calculated using Equation 6 with the inputs illustrated in Figures 1c and 2b.

In the 3-D problem of the AGW generation, the spatial spectrum of vibrations is affected by the finite extent of the ice shelf along the ice front. We obtain

$$\Phi(k_x, k_y) = \frac{1}{\pi k_y}\Phi_1(k_x)\sin\left(\frac{k_y L_y}{2}\right). \tag{28}$$

from Equations 2 and 22. Here Φ_1 is the spectrum in the 2-D model, Equation 25. Note that $\Phi = 0$ at $k_x = 0$, and the average vertical displacement of the ice shelf remains 0 in the 3-D problem.

When $\xi_{1,2}L \gg 1$, which corresponds to higher-order vibration modes, the dependence of $\Phi_1(k_x)$ and $\Phi(k_x, k_y)$ on k_x has sharp, delta function-like peaks at $k_x = \pm\xi_1$ and $k_x = \pm\,\xi_2$. Shape of the spectrum $\Phi_1(k_x)$ Equation 25 for the low-order modes, which are of primary interest in this work, is illustrated in Figure 1c. The RIS parameters assumed in the calculation are $L = 550$ km, $L_y = 800$ km, $H_1 = 300$ m, $H_2 = 400$ m, and $\rho_2/\rho_1 = 0.9$. For illustration purposes, we choose one of the natural frequencies of RIS oscillations, $\omega = 5.66317{\cdot}10^{-4}$ s^{-1}, which is obtained by solving Equation 24.

3.2. Vertical Cross-Section of the AGW Wave Field

The response of the polar atmosphere to vibrations of the RIS is illustrated in Figure 2. The atmospheric conditions are chosen to represent one day, 14 July 2014, during the Antarctic winter and are illustrated in Figure 2a. Atmospheric waves are modeled in the vertical plane $y = 0$ through the center of the ice front using the integral representation Equation 6 for the AGW field. The atmosphere is forced by a single normal mode of the RIS vibrations with the spatial spectrum illustrated in Figure 1c. The period of this mode and the linear AGWs it generates is $2\pi/\omega \approx 3.0819$ hr. For the linear waves we consider, response of the atmosphere to the ground level vibrations represented by a set of normal modes of various amplitudes is given by a corresponding superposition of the AGW fields generated by each individual mode.

The vertical displacement $W(\mathbf{k}, z)$ in Equation 6 has been calculated as a numerical solution of the one-dimensional AGW wave Equation 15 written in terms of the normalized displacement Q defined in Equation 17. In describing the wave dissipation, we disregarded the contribution of the bulk viscosity in Equation 12 for M and used the Eucken expression for thermal conductivity and the Sutherland equation for shear viscosity (Sutherland & Bass, 2004). For the quasi-plane waves that have critical levels, the numerical solution was terminated at some altitude $z = H$ slightly below the lowest critical level, see Section 2.4. A small positive imaginary part was added

to the wave frequency ω, as discussed in Section 2.4, to suppress non-causal artifacts in the numerical solution of the wave equation. Since $\Phi_1(0) = 0$ in the integrand in the right side of Equation 6 [see Equation 27], the waves with small values of k_x contribute negligibly to the integral. That allowed us to avoid the unnecessary calculation of $W(\mathbf{k}, z)$ for very long quasi-plane waves with the trace speeds of hundreds of m/s. The result of calculation of the vertical displacement in quasi-plane waves is illustrated in Figure 2b. The color in Figure 2b shows the amplitude of the normalized vertical displacement Q in a quasi-plane wave, Equation 17, on the logarithmic scale as $\log_{10}|Q|$. The sudden transitions between large and very small (zero) amplitudes of the normalized displacement at certain altitudes in Figure 2b correspond to the termination of the computational domain in the vicinity of the corresponding critical levels. Zero amplitude is also shown in the figure in the narrow band around $k_x = 0$, where $W(\mathbf{k}, z)$ calculation was not needed.

The full wave field, which is obtained by integration over the horizontal wavenumber k_x in Equation 6, is illustrated in Figure 2c. In that figure, color shows the amplitude of the normalized vertical displacement of the full AGW field on a logarithmic scale as $0.5\log_{10}[\rho(z)|w(x,z)|^2/\rho(0)]$ with an arbitrarily chosen amplitude A of the RIS vibrations in Equation 22.

The wave field appears to be a superposition of several wave beams associated with various peaks of the spatial spectrum of the vertical displacement of the ice surface, see Figure 1c. Various wave beams are refracted differently due to temperature and wind velocity gradients and can even cross each other (Figure 2c). The wave amplitude tends to decrease with altitude due to the critical level filtering, geometrical spreading of the beams, and the wave dissipation, which accelerates with increasing z. However, a localized increase in the amplitude due to wave focusing by refraction can also be seen in Figure 2c. This focusing is unrelated to the well-known vertical displacement amplification with decreasing air density as the latter effect is compensated for in the normalized displacement.

Figure 2c shows that, for the atmospheric stratification shown in Figure 2a, most (but not all) of the energy radiated by the RIS vibrations propagates at a small angle to the horizontal plane and can travel 1,000 km horizontally by the time it reaches the 20 km altitude. These features of Figure 2c suggest that, in addition to the RIS vibrations, oscillations of another ice shelf, for example, the Ronne Ice Shelf (Jenkins & Doake, 1991), the center of which is located about 1,500 km from the RIS center, can contribute to generation of the atmospheric waves observed at altitudes from about 20 km above the RIS.

Our model of the AGW generation is linear, and the results shown in Figure 2c do not include any nonlinear wave interactions. The main nonlinear effect is generation of secondary atmospheric waves above the critical level of primary AGWs due to the momentum and energy deposited near the critical level by the dissipating primary waves (Vadas et al., 2018). In addition to the waves generated by the ice shelf vibrations, the atmospheric wave field in the RIS vicinity is likely to include the nonlinearly generated secondary waves as well as linear waves that traveled to the region from sources outside the RIS.

The calculations illustrated in Figure 2 can be readily extended at a small additional computational cost to a different spatial structure of vibrations of the lower boundary of the atmosphere as long as the vibrations' frequency remains the same. The bulk of the computational effort is in solving the one-dimensional wave equation for various horizontal wavenumbers. Calculating the Fourier integral in Equation 6 with a new spatial spectrum $\Phi_1(k_x)$ of the ground-level vertical displacement is relatively quick, even for a large set of altitudes.

3.3. Three-Dimensional Structure of the Wave Field in the Atmosphere

The multiple peaks in the spatial spectrum of RIS vibrations (Figure 1c) and the anisotropic nature of AGW propagation can result in a rather complex three-dimensional distribution of wave energy in the atmosphere. To separate the effects of the wind-induced horizontal anisotropy from the effects of atmospheric stratification, in this section we assume that the atmosphere is isothermal, and the wind velocity is uniform.

In isothermal atmosphere with uniform wind, rays are straight lines. For any horizontal wave vector $\mathbf{k} = (k_x, k_y, 0) = k\,(\cos\psi, \sin\psi, 0)$, the ray direction is given by Equation 10 for the group speed $\mathbf{c}_g = (c_{g\,x}, c_{g\,y}, c_{g\,z})$. The rays emanating from a point $(x_0, y_0, 0)$ are given by the following equations: $x = x_0 + zc_{gx}/c_{gz}, y = y_0 + zc_{gy}/c_{gz}$. Let the wind velocity have no y component. In terms of the x-component of the horizontal wave vector and the angle ψ that $\mathbf{k}$ makes with the x coordinate axis, the ray equations become

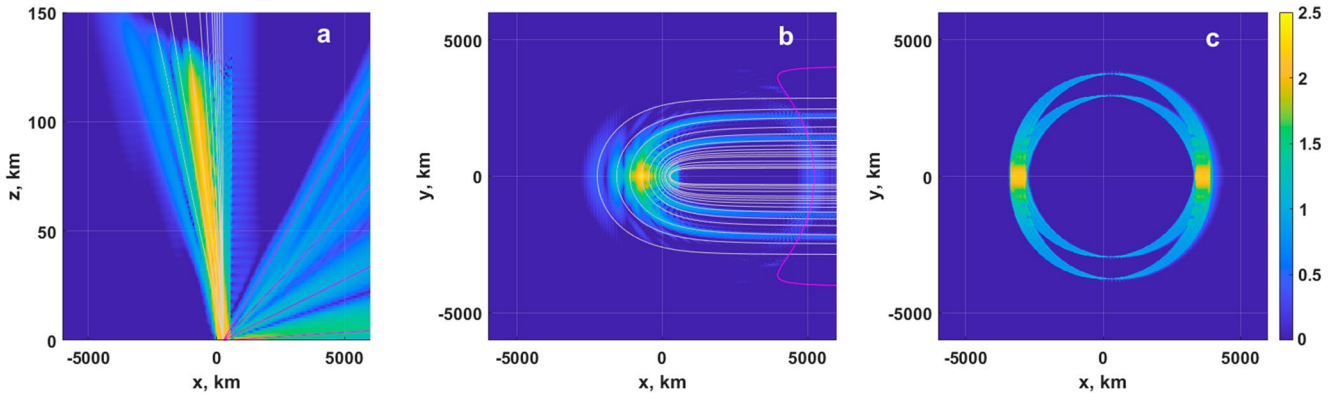

Figure 3. Radiation of AGWs by RIS vibrations into an isothermal atmosphere. The amplitude of the normalized vertical displacement is shown by color on a logarithmic scale. (a) Vertical cross-section of the wave field in the direction parallel to the wind velocity. Wind velocity is 10 m/s in the positive x direction. The RIS vibrations are due to a single normal mode with the spatial spectrum shown in Figure 1c. Thin colored lines show the AGW rays emitted from the center of RIS in the xz plane with the values of the k_x component of the wave vector representing various peaks of the spatial spectrum of RIS oscillations that is shown in Figure 1c. The line color is the same as the color of the corresponding dot in Figure 1c. (b) Horizontal cross-section of the wave field at the altitude $z = 100$ km under the same conditions as in (a). Thin colored lines show intersections of the plane $z = 100$ km with the AGW rays emitted from the center of RIS with various values of the k_y component of the wave vector and the k_x component representing one of the peaks of the spatial spectrum of the RIS oscillations that is shown in Figure 1c. The line color is chosen in the same way as in (a). (c) Same as in (b) but in the absence of wind.

$$x = x_0 + \frac{z}{|m|}\left[k_x\frac{N_0^2-\omega_d^2}{\omega_d^2} + \frac{k_x^2 u_x N_0^2}{\omega_d^3\cos^2\psi} - \frac{u_x\omega_d}{c^2}\right], y = y_0 + \frac{k_x z\left(N_0^2-\omega_d^2\right)\tan\psi}{|m|\omega_d^2}. \quad (29)$$

according to Equations 10 and 11.

In stationary atmosphere, according to Equation 29, the rays launched in different azimuthal directions ψ from a monochromatic source of frequency $\omega < N_0$ intersect the horizontal plane z = const. along a circle with the center right above the source and the radius $|m|^{-1}k\left(\omega^{-2}N_0^2-1\right)z$. When the trace speed is small compared to the sound speed, $k \gg \omega/c$, and the radius becomes $\left(\omega^{-2}N_0^2-1\right)^{1/2}z$, according to the dispersion Equation 7. Hence, all AGWs of frequency ω (and with small trace velocities) propagate at the same angle with the horizontal plane. The angle is small for low-frequency waves with $\omega \ll N_0$.

In moving atmosphere ($u_x \neq 0$), Equation 29 shows that the rays with different k_x values make different angles with the horizontal plane, and intersect the z = const. plane along a line, which goes to infinity in the downwind direction (Figure 3).

The three-dimensional structure of the atmospheric wave field generated by a single mode of RIS vibrations with period of about 3.0819 hr is illustrated in Figure 3. The figure shows the distribution of the amplitude of the normalized vertical displacement in horizontal and vertical planes. As in Figure 2c, the color in Figure 3 shows the amplitude of the normalized vertical displacement on logarithmic scale, namely, $0.5\log_{10}[\rho(z)|w(x,y,z)|^2/\rho(0)]$. The amplitude A of the RIS vibrations in Equation 22 is chosen arbitrarily. Figure 3a assumes the same RIS oscillations and serves as the counterpart of Figure 2b but from a full 3-D model in the simpler case of an isothermal atmosphere. The vertical displacement $w(x, z)$ is calculated using the integral representation Equation 3. Significant savings in the computation time are achieved by analytically calculating the function W in the integrand. As long as AGW dissipation is negligible, the exact solution of the boundary value problem for W is $W(\mathbf{k},z) = \exp(-il_m|z)$ in the isothermal atmosphere with uniform wind. The dissipation is included in this solution through Equations 8 and 12 as the additional factor $\exp\left(-\int_0^z |M/2m|dz\right)$. This is consistent with using the WKB Equation 8 and replacing m with $m_e \approx m + iM/2m$ in the phase integral Equation 9.

It is assumed in Figures 3a and 3b that the wind velocity has no y component and $u_x = 10$ m/s. For comparison, wind velocity $\mathbf{u} = 0$ in Figure 3c. We interpret the uniform wind $\mathbf{u}$ as the limiting case of a rapid rise of the x component of the wind velocity from 0 at $z = 0$ to u_x at $z > 0$. Then, the critical level filtering removes contributions of waves with $k_x > \omega/u_x$ into the integral Equation 3 in the calculations illustrated in Figures 3a and 3b.

In the vertical plane $y = 0$ (Figure 3a), the more significant maxima of the AGW amplitude in the full-wave simulation occur along the rays corresponding to those local maxima of the spectrum of RIS oscillations $\Phi_1(k_x)$ Equation 25 that produce atmospheric waves with the intrinsic frequency $\omega_d > 0$ and thus contribute to the field at $z > 0$. At $y = 0$, significant contributions to the integral in Equation 3 over k_y come from the vicinity of $k_y = 0$, where the magnitude of the spectrum $\Phi(k_x, k_y)$ in Equation 28 is maximum. The finite width of the "wave beams" that are seen in Figure 3a around the rays originates from the finite linear dimensions of RIS and the resulting finite width of the spectral maxima. Figure 3a shows that some wave energy travels upwards at near-vertical angles in the atmosphere even at a wave frequency much lower than the buoyancy frequency. This point is important for interpretation of the observations (Chen et al., 2016; Chu et al., 2018; Kim et al., 2022; Kwon et al., 2018; Zabotin et al., 2023; Zhao et al., 2017) and is elaborated upon in Section 4.

In the horizontal cross-section of the AGW field in motionless atmosphere (Figure 3c) it is easy to recognize the circles that are discussed above in the ray context. The energy of the long-period RIS oscillations is concentrated at wavenumbers large compared to $\omega/c \sim 2{\cdot}10^{-6}$ m^{-1} (Figure 1c), and therefore AGWs with different wave vectors propagate at the same angle to the vertical. The circle radius in the wave field distribution in Figure 3c is consistent with the ray calculation, and the apparent shift of the circles is of the order of the RIS linear dimensions. The azimuthal distribution of the amplitude can be thought of as a result of interference of waves arriving from different parts of the RIS, but it is best understood in terms of the spectrum $\Phi(k_x, k_y)$ in Equation 28. In the absence of wind, the azimuthal direction of wave propagation is parallel to the horizontal wave vector $\mathbf{k}$. In Figure 3c, the AGW amplitude is largest along the x axis, where wave vectors have small k_y values and $|\Phi(k_x, k_y)|$ is close to its maximum. The wave amplitude is much smaller around the y axis, where wave vectors have small k_x values, because $\Phi(0, k_y) = 0$ according to Equations 27 and 28.

In the moving atmosphere (Figure 3b), the effects of the wave source directionality, which are encapsulated in the spectrum $\Phi(k_x, k_y)$, combine with the horizontal anisotropy of AGW propagation to produce a more intricate dependence of the wave field on horizontal coordinates than in Figure 3c. The spectrum $\Phi(k_x, k_y)$ of the RIS vibrations varies rapidly with k_x and has multiple local maxima at specific k_x values, while variation of the spectrum with k_y is much more gradual in Equation 28. The ice shelf radiates a number of wave beams, each one being associated with a local maximum of $|\Phi_1(k_x)|$. Different beams travel upwards in different directions. With k_x fixed and the angle ψ varying from 0 to 2π, Equation 29 defines the line, along which the beam intersects the horizontal plane at the altitude z. Largest amplitudes of the wave field in Figure 3b occur in bands along the lines predicted by Equations 25 and 29. For each beam, the AGW amplitude in Figure 3b is largest around $y = 0$ and decreases with increasing $|y|$. The amplitude decreases, first, because of the decrease of $|\Phi(k_x, k_y)|$ with increasing $|k_y|$ (i.e., due to the source directionality) and, second, because the energy in a fixed interval of k_y values spreads over a larger area in the horizontal plane as $|y|$ increases (i.e., due to geometrical spreading of the beam).

Comparison of Figures 3b and 3c shows that the maximum of the AGW energy is expected to be observed much closer to the RIS in moving atmosphere than in the motionless case. Moreover, Figure 3b shows significant AGW amplitudes directly above the RIS at 100 km altitude. These properties of the simulated AGW field provide a physical explanation of the recently reported observations (Zabotin et al., 2023) of the correlations between the seismometer-measured vertical displacements of the top surface of the RIS and HF radar measurements of the thermospheric wave activity at the Antarctic Jang Bogo Station, which is located at the distance of approximately 500 km from the edge of the RIS.

4. Short, Low-Frequency AGWs

Persistent atmospheric wave activity with wave periods of several hours is observed in the middle and upper atmosphere above and close to RIS (Chen et al., 2016; Chu et al., 2018; Kim et al., 2022; Kwon et al., 2018; Zabotin et al., 2023; Zhao et al., 2017). At such wave periods, as illustrated in Figure 3c, AGWs propagate in near-horizonal directions in a windless atmosphere (Gossard & Hooke, 1975), which seems to suggest that the waves were generated at large horizontal distances from the observation point. In fact, near-zenith AGW propagation can result from a particular wind profile, see Equation 11. In this section, we consider short AGWs on the gravity branch of the AGW dispersion curve (i.e., with intrinsic frequencies $0 < \omega_d < N_0$) and show that, at least for short waves, propagation in near-zenith direction can occur even when wind velocity does not change with altitude.

4.1. Stationary Atmosphere, Moderate Winds, or Down-Wind Propagation of Short AGWs

Assume that the intrinsic frequency ω_d of an atmospheric wave is of the same order of magnitude, or less than, ω. This is always the case for waves propagating down-wind (more accurately, for the AGWs with $\mathbf{k}\cdot\mathbf{u} \geq 0$), the intrinsic frequency of which varies between ω in the absence of wind and 0 at the critical level. In the limit of large k, the dispersion Equation 7 becomes

$$m^2 = k^2\left(N_0^2 - \omega_d^2\right)/\omega_d^2. \tag{30}$$

In this regime, $m^2 > 0$ and there are no turning points. Both k and m^2 are "large." Quantitatively, Equation 30 is a good approximation when

$$m^2 h^2 \gg 1. \tag{31}$$

The approximate dispersion Equation 30 is similar to the often-used "dispersion equation of moderate-frequency gravity waves" (Fritts & Alexander, 2003). For the persistent wave activity observed at McMurdo, Antarctica, the assumption Equation 31 is very well satisfied at stratospheric altitudes (Zhao et al., 2017) and is approximately satisfied in the mesosphere and lower thermosphere (Chen et al., 2016).

The frequencies ω of interest in the RIS problem are much smaller than N_0. (For orientation, for the 3-hr wave period $T = 2\pi/\omega$, we have $N_0/\omega \sim 30$–40.) Then $m^2 \gg k^2$ according to Equation 30, and from Equation 10 for the group speed we find

$$\mathbf{c}_g = \mathbf{u} + \omega_d\left(k^{-2}\mathbf{k} - m^{-1}\hat{\mathbf{z}}\right). \tag{32}$$

Equation 32 shows that, in the reference frame moving with the local wind, the ratio of the horizontal and vertical components of the group speed is $|m|/k \gg 1$, that is, the AGWs propagate nearly horizontally making the angle $\arctan(k/|m|) \sim \omega/N_0 \ll 1$ with the horizontal plane.

It follows from Equation 32 that

$$\mathbf{c}_g \cdot \mathbf{k}/k = \omega/k = V \tag{33}$$

in this approximation, where V is the trace velocity. Hence, the projection of the group speed on the direction of $\mathbf{k}$ (which equals the horizontal component of group speed in the 2-D problem and, in the absence of the transverse wind, also in the 3-D case) coincides with the trace speed and does not change with altitude. It follows from Equations 32 and 33 that, in the reference frame of the solid ground,

$$\frac{(c_g)_z}{\mathbf{c}_g \cdot \mathbf{k}/k} = -\frac{\omega_d k}{\omega m}. \tag{34}$$

Thus, the ratio of the vertical and horizontal components of the group speed remains small and of the same order of magnitude as in the moving reference frame.

In the absence of winds, the ratio of the vertical and horizontal components equals $k/|m|$ and, according to Equation 30, depends only on the wave frequency, that is, waves of frequency ω with different V and k propagate in the same direction. With wind, the directions are no longer exactly the same for waves with different k (or V); but the ratios $k/|m|$ for these waves are still small and of the same order of magnitude.

4.2. Upwind Propagation of Short AGWs

The analysis in Section 4.1 assumes that ω_d is of the same order of magnitude, or less than, ω. Now, consider the opposite case, where $\omega_d \gg \omega$. This situation occurs, when slow atmospheric waves propagate upwind, more precisely, when the wind velocity component in the direction of vector $\mathbf{k}$, $u_k = \mathbf{k}\cdot\mathbf{u}$, is negative and has the magnitude large compared to the trace speed $V = \omega/k$. Then we have, approximately,

$$\omega_d = k|u_k|. \tag{35}$$

Given prevailing wind speeds of tens of m/s in a wide range of altitudes of polar atmosphere, this is not an exceptional regime for AGWs with $V < 10$ m/s as long as the wind direction is not reversed with altitude. (As

previously discussed, AGWs with $V < 10$ m/s and even larger V are absorbed in the vicinity of their critical levels at propagation downwind from the sources located at the ground level.) Short AGWs with $\omega \ll \omega_d < N_0$ prove to have rather different properties than those discussed in Section 4.1.

Substitution of Equation 35 into the dispersion Equation 7 gives

$$m^2 = \frac{N_0^2}{u_k^2} - \frac{1}{4h^2} - k^2\left(1 - \frac{u_k^2}{c^2}\right). \tag{36}$$

Note that, unlike Equation 30, m^2 decreases with increasing k^2, as for acoustic waves, and that short waves can have turning points, provided $|u_k| < 2hN_0$. The latter condition reduces to $|u_k|/c < 2\sqrt{\gamma - 1}/\gamma \approx 0.9$ and is always met in the atmosphere.

Let us now additionally assume that ω_d remains small compared to N_0:

$$\omega \ll k|u_k| \ll N_0. \tag{37}$$

We also assume for simplicity that ${u_k}^2 \ll c^2$. It follows from Equation 36 that

$$m^2 = N_0^2/u_k^2 \tag{38}$$

in this approximation. Then inequality (31) holds and $m^2 \gg k^2$according to Equation 37. From Equation 10 for the group speed we find

$$\mathbf{c}_g \cdot \frac{\mathbf{k}}{k} = \frac{k^2 u_k^3}{N_0^2} = -|u_k|\frac{\omega_d^2}{N_0^2}. \tag{39}$$

Direction of the horizontal component of the group speed is opposite to the direction of $\mathbf{k}$ in Equation 39; while the wave vector is directed upwind, wave energy travels downwind. Under conditions (37), the vertical component of the group speed in Equation 10 becomes

$$(c_g)_z = -|u_k^3|\frac{mk}{N_0^2} = -|u_k|\frac{m}{k}\frac{\omega_d^2}{N_0^2}, \tag{40}$$

and

$$\left|\frac{(c_g)_z}{\mathbf{c}_g \cdot \mathbf{k}/k}\right| = \frac{|m|}{k} \gg 1. \tag{41}$$

Hence, the wave propagates almost vertically. This is in contrast to near-horizontal propagation found in Section 4.1, see Equation 34.

We conclude that short AGWs with trace velocities V within about 10 m/s directed upwind can provide a mechanism for transporting wave energy from RIS vibrations into middle atmosphere at observation points right above RIS.

A simple result for the group speed direction can also be obtained under somewhat relaxed assumptions. Now, we no longer assume validity of Equation 37 and allow $k|u_k|$ to be as large as N_0. Then, from Equation 36 we have the approximate dispersion equation

$$m^2 = \frac{N_0^2}{u_k^2} - k^2 \tag{42}$$

instead of Equation 38, and the relative magnitude of m^2 and k^2 can be arbitrary. Using Equations 10 and 42, for the group speed and its components we find

$$\mathbf{c}_g = \mathbf{u} - \frac{m^2 k u_k}{k^2 + m^2}\left(\frac{\mathbf{k}}{k^2} - \frac{\hat{\mathbf{z}}}{m}\right), \tag{43}$$

$$\mathbf{c}_g \cdot \frac{\mathbf{k}}{k} = \frac{k^2 u_k}{k^2 + m^2} = -\frac{k^2 |u_k^3|}{N_0^2}, \frac{(c_g)_z}{\mathbf{c}_g \cdot \mathbf{k}/k} = \frac{m}{k}. \quad (44)$$

Equations 39–41 are recovered from Equations 43 and 44 when $m^2 \gg k^2$. It should be emphasized, again, that the result (Equation 44) for the group speed direction is similar in appearance but opposite to the prediction of Equation 34, which is valid in the case of weak winds with $|u_k| < V$. When $m^2 \gg k^2$, Equations 44 and 34 indicate near-vertical and near-horizontal propagation, respectively, for the same, near-horizontal orientation of the AGW wave fronts, that is, surfaces of constant wave phase.

5. Concluding Remarks

An efficient quantitative description of the waves generated in a stratified atmosphere by distributed and/or directional wave sources can be achieved by a Fourier synthesis of waves with harmonic dependence on horizontal coordinates. This approach is superior to representing the distributed source as a superposition of point sources, because AGW Green's functions have singularities away from the point source (Adam, 1977) and are numerically expensive to calculate in an inhomogeneous, moving atmosphere. We have extended to atmospheric AGWs the wavenumber integration method, a full-field approach that was originally developed for sound and seismic waves. In contrast to acoustic and seismic applications, the integration domain in the wavenumber space is primarily restricted by the AGW absorption and critical level filtering in the atmosphere rather than by the waves with short horizontal wavelengths becoming evanescent.

The approach developed in this paper provides the AGW field in a wide spatial domain and is particularly suitable for modeling the background wave activity (the "geophysical noise"), against which the atmospheric manifestations of earthquakes, tsunamis, and other transient events (Artru et al., 2005; Astafyeva et al., 2013; Garcia et al., 2014; Hickey et al., 2009; Inchin et al., 2021; Maruyama et al., 2012; Meng et al., 2019) are to be detected. This work has focused on waves generated by vibrations of the lower boundary of the atmosphere, but the numerical model can be readily extended to include waves generated in the atmosphere by using previously obtained spectral representations of the field due to various compact or distributed wave sources (e.g., Godin & Fuks, 2012; Kanamori et al., 1994; Pierce, 1963; Watada & Kanamori, 2010).

The linear response of the polar atmosphere to free vibrations of the RIS has been quantified by using the wavenumber integration approach and a previously developed model of the long-period vibrations of ice shelves (Godin & Zabotin, 2016). Each normal mode of the RIS vibrations generates an intricate, unique wave pattern from the ground level to the middle and upper atmosphere. Remarkably, the AGWs due to the RIS vibrations with natural frequencies that are small compared to the buoyancy frequency, propagate in a wide range of directions from near-horizontal to near-vertical in an atmosphere with moderate winds. Distribution of the wave energy in the horizontal plane is dramatically different in the moving and stationary atmospheres. The predicted amplitude of the atmospheric waves and the spatial structure of the AGW field are controlled by the temporal and spatial spectra of the atmospheric forcing by the RIS, which determine the wave source directionality and affect the AGW diffraction, and by the variations of the temperature and wind velocity with altitude, which influence the AGW refraction and dissipation.

Data Availability Statement

The data used in this research were obtained from the models HWM14 and NRLMSISE-00.2 (Drob et al., 2015; Picone et al., 2002) as detailed in Figure 2 caption.

Acknowledgments
The research reported in this paper was supported by the National Science Foundation, award OPP-1643119. The authors are grateful to three anonymous reviewers for their thoughtful comments and suggestions, which helped us to improve the presentation.

References

Adam, J. A. (1977). Solutions of the inhomogeneous acoustic-gravity wave equation. *Journal of Physics A: Mathematical and General*, *10*(9), L169–L173. https://doi.org/10.1088/0305-4470/10/9/006

Aki, K., & Richards, P. (2002). *Quantitative seismology: Theory and methods* (2nd ed., p. 718). University Science Books.

Alexander, S. P., Sato, K., Watanabe, S., Kawatani, Y., & Murphy, D. J. (2016). Southern Hemisphere extratropical gravity wave sources and intermittency revealed by a middle-atmosphere general circulation model. *Journal of the Atmospheric Sciences*, *73*(3), 1335–1349. https://doi.org/10.1175/jas-d-15-0149.1

Artru, J., Ducic, V., Kanamori, H., Lognonné, P., & Murakami, M. (2005). Ionospheric detection of gravity waves induced by tsunamis. *Geophysical Journal International*, *160*(3), 840–848. https://doi.org/10.1111/j.1365-246X.2005.02552.x

Astafyeva, E., Rolland, L., Lognonné, P., Khelfi, K., & Yahagi, T. (2013). Parameters of seismic source as deduced from 1 Hz ionospheric GPS data: Case study of the 2011 Tohoku-Oki event. *Journal of Geophysical Research: Space Physics*, *118*(9), 5942–5950. https://doi.org/10.1002/jgra.50556

Averbuch, G., Assink, J. D., & Evers, L. G. (2020). Long-range atmospheric infrasound propagation from subsurface sources. *Journal of the Acoustical Society of America*, *147*(2), 126474–131274. https://doi.org/10.1121/10.0000792

Brekhovskikh, L. M., & Godin, O. A. (1999). *Acoustics of layered media 2: Point sources and bounded beams* (2nd ed., p. 540). Springer.

Bromirski, P. D., Diez, A., Gerstoft, P., Stephen, R. A., Bolmer, T., Wiens, D. A., et al. (2015). Ross ice shelf vibrations. *Geophysical Research Letters*, *42*(18), 7589–7597. https://doi.org/10.1002/2015GL065284

Budden, K. G., & Smith, M. S. (1976). Phase memory and additional memory in WKB solutions for wave propagation in stratified media. *Proceedings of the Royal Society of London A*, *350*(1660), 27–46.

Chen, C., Chu, X., Zhao, J., Roberts, B. R., Yu, Z., Fong, W., et al. (2016). Lidar observations of persistent gravity waves with periods of 3–10 h in the Antarctic middle and upper atmosphere at McMurdo (77.83°S, 166.67°E). *Journal of Geophysical Research: Space Physics*, *121*(2), 1483–1502. https://doi.org/10.1002/2015JA022127

Chu, X., Zhao, J., Lu, X., Harvey, V. L., Jones, R. M., Becker, E., et al. (2018). Lidar observations of stratospheric gravity waves from 2011 to 2015 at McMurdo (77.84°S, 166.69°E), Antarctica: 2. Potential energy densities, lognormal distributions, and seasonal variations. *Journal of Geophysical Research: Atmospheres*, *123*(15), 7910–7934. https://doi.org/10.1029/2017JD027386

Diez, A., Bromirski, P. D., Gerstoft, P., Stephen, R. A., Anthony, R. E., Aster, R. C., et al. (2016). Ice shelf structure derived from dispersion curve analysis of ambient seismic noise, Ross Ice Shelf, Antarctica. *Geophysical Journal International*, *205*(2), 785–795. https://doi.org/10.1093/gji/ggw036

DiNapoli, F. R., & Deavenport, R. L. (1980). Theoretical and numerical Green's function field solution in a plane multilayered medium. *Journal of the Acoustical Society of America*, *67*(1), 92–105. https://doi.org/10.1121/1.383794

Drob, D. P., Emmert, J. T., Meriwether, J. W., Makela, J. J., Doornbos, E., Conde, M., et al. (2015). An update to the horizontal wind model (HWM): The quiet time thermosphere. *Earth and Space Science*, *2*(7), 301–319. https://doi.org/10.1002/2014EA000089

Einaudi, F., & Hines, C. O. (1970). WKB approximation in application to acoustic-gravity waves. *Canadian Journal of Physics*, *48*(12), 1458–1471. https://doi.org/10.1139/p70-185

Fritts, D. C., & Alexander, M. J. (2003). Gravity wave dynamics and effects in the middle atmosphere. *Reviews of Geophysics*, *41*(1), 1003. https://doi.org/10.1029/2001rg000106

Fuchs, K., & Müller, G. (1971). Computation of synthetic seismograms with the reflectivity method and comparison with observations. *Geophysical Journal International*, *23*(4), 417–433. https://doi.org/10.1111/j.1365-246x.1971.tb01834.x

Garcia, R. F., Doornbos, E., Bruinsma, S., & Hebert, H. (2014). Atmospheric gravity waves due to the Tohoku-Oki tsunami observed in the thermosphere by GOCE. *Journal of Geophysical Research: Atmospheres*, *119*(8), 4498–4506. https://doi.org/10.1002/2013jd021120

Geller, M. A., Alexander, M. J., Love, P. T., Bacmeister, J., Ern, M., Hertzog, A., et al. (2013). A comparison between gravity wave momentum fluxes in observations and climate models. *Journal of Climate*, *26*(17), 6383–6405. https://doi.org/10.1175/jcli-d-12-00545.1

Godin, O. A. (1984). Diffraction theory of bounded wave beams displacement at reflection, Part 1. *Zhurnal Tekhnicheskoi Fiziki*, *54*(11), 2094–3004.

Godin, O. A. (1997). Reciprocity and energy theorems for waves in a compressible inhomogeneous moving fluid. *Wave Motion*, *25*(2), 143–167. https://doi.org/10.1016/S0165-2125(96)00037-6

Godin, O. A. (2012). Acoustic-gravity waves in atmospheric and oceanic waveguides. *Journal of the Acoustical Society of America*, *132*(2), 657–669. https://doi.org/10.1121/1.4731213

Godin, O. A. (2014). Dissipation of acoustic-gravity waves: An asymptotic approach. *Journal of the Acoustical Society of America*, *136*(6), EL411–EL417. https://doi.org/10.1121/1.4902426

Godin, O. A. (2015). Wentzel–Kramers–Brillouin approximation for atmospheric waves. *Journal of Fluid Mechanics*, *777*, 260–290. https://doi.org/10.1017/jfm.2015.367

Godin, O. A., & Fuks, I. M. (2012). Transmission of acoustic-gravity waves through gas–liquid interfaces. *Journal of Fluid Mechanics*, *709*, 313–340. https://doi.org/10.1017/jfm.2012.336

Godin, O. A., & Zabotin, N. A. (2016). Resonance vibrations of the Ross Ice Shelf and observations of persistent atmospheric waves. *J. Geophys. Res. – Space Phys.*, *121*(10), 10157–10171. https://doi.org/10.1002/2016ja023226

Godin, O. A., Zabotin, N. A., & Bullett, T. W. (2015). Acoustic-gravity waves in the atmosphere generated by infragravity waves in the ocean. *Earth Planets and Space*, *67*(1), 47. https://doi.org/10.1186/s40623-015-0212-4

Godin, O. A., Zabotin, N. A., & Zabotina, L. (2020). Atmospheric resonances and their coupling to vibrations of the ground and waves in the ocean. *Earth Planets and Space*, *72*(1), 125. https://doi.org/10.1186/s40623-020-01260-9

Golitsyn, G. S. (1965). Damping of small oscillations in the atmosphere due to viscosity and thermal conductivity. *Izvestiya Academy of Sciences USSR, Atmospheric and Oceanic Physics*, *1*, 82–89.

Gossard, E. E., & Hooke, W. H. (1975). *Waves in the atmosphere* (p. 456). Elsevier.

Hickey, M. P., Schubert, G., & Walterscheid, R. L. (2009). The propagation of tsunami-driven gravity waves into the thermosphere and ionosphere. *Journal of Geophysical Research*, *114*(A8), A08304. https://doi.org/10.1029/2009JA014105

Hines, C. O. (1960). Internal atmospheric gravity waves at ionospheric heights. *Canadian Journal of Physics*, *38*(11), 1441–1481. https://doi.org/10.1139/p60-150

Holdsworth, G., & Glynn, J. (1978). Iceberg calving from floating glaciers by a vibrating mechanism. *Nature*, *274*(5670), 464–466. https://doi.org/10.1038/274464a0

Holdsworth, G., & Glynn, J. E. (1981). A mechanism for the formation of large icebergs. *Journal of Geophysical Research*, *86*(NC4), 3210–3222. https://doi.org/10.1029/JC086iC04p03210

Hunsucker, R. D. (1982). Atmospheric gravity waves generated in the high-latitude ionosphere: A review. *Reviews of Geophysics*, *20*(2), 293–315. https://doi.org/10.1029/rg020i002p00293

Inchin, P. A., Snively, J. B., Kaneko, Y., Zettergren, M. D., & Komjathy, A. (2021). Inferring the evolution of a large earthquake from its acoustic impacts on the ionosphere. *AGU Advances*, *2*(2), e2020AV000260. https://doi.org/10.1029/2020av000260

Jenkins, A., & Doake, C. S. M. (1991). Ice-ocean interaction on Ronne Ice Shelf, Antarctica. *Journal of Geophysical Research*, *96*(C1), 791–813. https://doi.org/10.1029/90jc01952

Jensen, F. B., Kuperman, W. A., Porter, M. B., & Schmidt, H. (2011). *Computational ocean acoustics* (2nd ed., pp. 233–335). Springer.

Jones, M., & Georges, T. M. (1976). Infrasound from convective storms. III. Propagation to the ionosphere. *Journal of the Acoustical Society of America*, *59*(4), 765–779. https://doi.org/10.1121/1.380942

Kanamori, H., Mori, J., & Harkrider, D. G. (1994). Excitation of atmospheric oscillations by volcanic eruptions. *Journal of Geophysical Research*, *99*(B11), 21947–22196. https://doi.org/10.1029/94jb01475

Kim, E., Jee, G., Ham, Y.-B., Zabotin, N., Lee, C., Kwon, H.-J., et al. (2022). Assessment of polar ionospheric observations by VIPIR/Dynasonde at Jang Bogo Station, Antarctica: Part 1—Ionospheric densities. *Remote Sensing*, *14*(12), 2785. https://doi.org/10.3390/rs14122785.1

Kubota, T., Saito, T., & Nishida, K. (2022). Global fast-traveling tsunamis driven by atmospheric Lamb waves on the 2022 Tonga eruption. *Science*, *377*(6601), 91–94. https://doi.org/10.1126/science.abo4364

Kulichkov, S. N., Chunchuzov, I. P., Popov, O. E., Gorchakov, G. I., Mishenin, A. A., Perepelkin, V. G., et al. (2022). Acoustic-gravity Lamb waves from the eruption of the Hunga-Tonga-Hunga-Hapai Volcano, its energy release and impact on aerosol concentrations and tsunami. *Pure and Applied Geophysics*, *179*(5), 1533–1548. https://doi.org/10.1007/s00024-022-03046-4

Kwon, H. J., Lee, C., Jee, G., Ham, Y. B., Kim, J. H., Kim, Y. H., et al. (2018). Ground-based observations of the polar region space environment at the Jang Bogo Station, Antarctica. *Journal of Astronomy and Space Sciences*, *35*(3), 185–193.

Lin, J. T., Rajesh, P. K., Lin, C. C., Chou, M. Y., Liu, J. Y., Yue, J., et al. (2022). Rapid conjugate appearance of the giant ionospheric Lamb Wave signatures in the Northern Hemisphere after Hunga-Tonga Volcano eruptions. *Geophysical Research Letters*, *49*(8), e2022GL098222. https://doi.org/10.1029/2022gl098222

Lognonné, P. (2010). Seismic waves from atmospheric sources and atmospheric/ionospheric signatures of seismic waves. In *Infrasound monitoring for atmospheric studies* (pp. 281–304). Springer.

Maruyama, T., Tsugawa, T., Kato, H., Ishii, M., & Nishioka, M. (2012). Rayleigh wave signature in ionograms induced by strong earthquakes. *Journal of Geophysical Research*, *117*(A8), A08306. https://doi.org/10.1029/2012JA017952

Matoza, R. S., Fee, D., Assink, J. D., Iezzi, A. M., Green, D. N., Kim, K., et al. (2022). Atmospheric waves and global seismoacoustic observations of the January 2022 Hunga eruption, Tonga. *Science*, *377*(6601), 95–100. https://doi.org/10.1126/science.abo7063

Medvedev, A. S., Klaassen, G. P., & Yiğit, E. (2023). On the dynamical importance of gravity wave sources distributed over different heights in the atmosphere. *Journal of Geophysical Research: Space Physics*, *128*(3), e2022JA031152. https://doi.org/10.1029/2022ja031152

Meng, X., Vergados, P., Komjathy, A., & Verkhoglyadova, O. (2019). Upper atmospheric responses to surface disturbances: An observational perspective. *Radio Science*, *54*(11), 1076–1098. https://doi.org/10.1029/2019rs006858

Occhipinti, G., Lognonne, P., Kherani, E. A., & Hebert, H. (2006). Three-dimensional waveform modeling of ionospheric signature induced by the 2004 Sumatra tsunami. *Geophysical Research Letters*, *33*(20), L20104. https://doi.org/10.1029/2006GL026865

Oyama, S., & Watkins, B. J. (2012). Generation of atmospheric gravity waves in the polar thermosphere in response to auroral activity. *Space Science Reviews*, *168*(1–4), 463–473. https://doi.org/10.1007/s11214-011-9847-z

Papathanasiou, T. K., Karperaki, A. E., & Belibassakis, K. A. (2019). On the resonant hydroelastic behaviour of ice shelves. *Ocean Modelling*, *133*, 11–26. https://doi.org/10.1016/j.ocemod.2018.10.008

Picone, J. M., Hedin, A. E., Drob, D. P., & Aikin, A. C. (2002). NRLMSISE-00 empirical model of the atmosphere: Statistical comparisons and scientific issues. *Journal of Geophysical Research*, *107*(A12), 1468. https://doi.org/10.1029/2002JA009430

Pierce, A. D. (1963). Propagation of acoustic-gravity waves from a small source above the ground in an isothermal atmosphere. *Journal of the Acoustical Society of America*, *35*(11), 1798–1807. https://doi.org/10.1121/1.1918824

Pierce, A. D. (2019). *Acoustics: An introduction to its physical principles and applications* (p. 678). Springer.

Pitteway, M. L. V., & Hines, C. O. (1965). The reflection and ducting of atmospheric acoustic–gravity waves. *Canadian Journal of Physics*, *43*(12), 2222–2243. https://doi.org/10.1139/p65-217

Plougonven, R., & Zhang, F. (2014). Internal gravity waves from atmospheric jets and fronts. *Reviews of Geophysics*, *52*(1), 33–76. https://doi.org/10.1002/2012rg000419

Press, F., & Harkrider, D. (1962). Propagation of acoustic-gravity waves in the atmosphere. *Journal of Geophysical Research*, *67*(10), 3889–3908. https://doi.org/10.1029/jz067i010p03889

Schmidt, H., & Glattetre, J. (1985). A fast field model for three-dimensional wave propagation in stratified environments based on the global matrix method. *Journal of the Acoustical Society of America*, *78*(6), 2105–2114. https://doi.org/10.1121/1.392670

Schmidt, H., & Tango, G. (1986). Efficient global matrix approach to the computation of synthetic seismograms. *Geophysical Journal of the Royal Astronomical Society*, *84*(2), 331–359. https://doi.org/10.1111/j.1365-246x.1986.tb04359.x

Sergienko, O. V. (2013). Normal modes of a coupled ice-shelf/sub-ice-shelf cavity system. *Journal of Glaciology*, *59*(213), 76–80. https://doi.org/10.3189/2013JoG12J096

Snively, J. B. (2013). Mesospheric hydroxyl airglow signatures of acoustic and gravity waves generated by transient tropospheric forcing. *Geophysical Research Letters*, *40*(17), 4533–4537. https://doi.org/10.1002/grl.50886

Sutherland, L. C., & Bass, H. E. (2004). Atmospheric absorption in the atmosphere up to 160 km. *Journal of the Acoustical Society of America*, *115*(3), 1012–1032. https://doi.org/10.1121/1.1631937

Vadas, S. L., Zhao, J., Chu, X., & Becker, E. (2018). The excitation of secondary gravity waves from local body forces: Theory and observation. *Journal of Geophysical Research: Atmospheres*, *123*(17), 9296–9325. https://doi.org/10.1029/2017jd027970

Vincent, R. A., Alexander, M. J., Dolman, B. K., MacKinnon, A. D., May, P. T., Kovalam, S., & Reid, I. M. (2013). Gravity wave generation by convection and momentum deposition in the mesosphere-lower thermosphere. *Journal of Geophysical Research: Atmospheres*, *118*(12), 6233–6245. https://doi.org/10.1002/jgrd.50372

Watada, S. (2009). Radiation of acoustic and gravity waves and propagation of boundary waves in the stratified fluid from a time-varying bottom boundary. *Journal of Fluid Mechanics*, *627*, 361–377. https://doi.org/10.1017/s0022112009005953

Watada, S., & Kanamori, H. (2010). Acoustic resonant oscillations between the atmosphere and the solid earth during the 1991 Mt. Pinatubo eruption. *Journal of Geophysical Research*, *115*(B12), 2319. https://doi.org/10.1029/2010jb007747

Wright, C. J., Hindley, N. P., Alexander, M. J., Barlow, M., Hoffmann, L., Mitchell, C. N., et al. (2022). Surface-to-space atmospheric waves from Hunga Tonga–Hunga Ha'apai eruption. *Nature*, *609*(7928), 741–746. https://doi.org/10.1038/s41586-022-05012-5

Wu, Y., Llewellyn Smith, S. G., Rottman, J. W., Broutman, D., & Minster, J.-B. H. (2020). Time-dependent propagation of tsunami-generated acoustic–gravity waves in the atmosphere. *Journal of the Atmospheric Sciences*, *77*(4), 1233–1244. https://doi.org/10.1175/jas-d-18-0322.1

Zabotin, N., Godin, O. A., Bromirski, P. D., Jee, G., Lee, W. S., Yun, S., & Zabotina, L. (2023). Low-frequency wave activity in the ocean - Ross Ice Shelf - Atmosphere system. *Earth and Space Science*, *10*(6), e2022EA002621. https://doi.org/10.1029/2022EA002621

Zabotin, N. A., Godin, O. A., & Bullett, T. W. (2016). Oceans are a major source of waves in the thermosphere. *Journal of Geophysical Research: Space Physics*, *121*(4), 3452–3463. https://doi.org/10.1002/2016ja022357

Zhao, J., Chu, X., Chen, C., Lu, X., Fong, W., Yu, Z., et al. (2017). Lidar observations of stratospheric gravity waves from 2011 to 2015 at McMurdo (77.84°S, 166.69°E), Antarctica: 1. Vertical wavelengths, periods, and frequency and vertical wave number spectra. *Journal of Geophysical Research: Atmospheres*, *122*(10), 5041–5062. https://doi.org/10.1002/2016JD026368